Physics in Medicine &
Biology

PAPER • **OPEN ACCESS**

Electron spin resonance measurements of radiation-induced radicals under conventional and ultra-high dose rate electron irradiation

To cite this article: Johanna Pehlivan *et al* 2026 *Phys. Med. Biol.* **71** 015016

View the article online for updates and enhancements.

You may also like

- Investigating radical yield variations in FLASH and conventional proton irradiation via microscopic Monte Carlo simulations
  Yuting Peng, Youfang Lai, Lingshu Yin et al.
- Pulse-by-pulse ultra-high resolution scintillation imaging of proton FLASH beams produced by a gantry-mounted synchrocyclotron
  S Murty Goddu, Scott Holloingsworth, Winter Green et al.
- Feasibility of prototype diamond detectors for pulsed UHDR PBS small-field proton dosimetry for proton FLASH experiments
  Jufri Setianegara, Aoxiang Wang, Nicolas Gerard et al.

physicsworld WEBINAR

ZAP-X radiosurgery & ZAP-Axon SRS planning

Technology Overview, Workflow, and Complex Case Insights from a Leading SRS Center

Get an inside look at European Radiosurgery Center Munich – a high-volume ZAP-X centre – with insights into its vault-free treatment suite, clinical workflow, patient volumes, and treated indications. The webinar will cover the fundamentals of the ZAP-X delivery system and what sets it apart from other SRS platforms; showcase real-world performance through complex clinical cases; and provide a concise overview of the recently unveiled next-generation ZAP-Axon radiosurgery planning system.

LIVE at 4 p.m. GMT/8 a.m. PST, 19 Feb 2026

Click to register

This content was downloaded from IP address 193.174.53.84 on 13/02/2026 at 10:19

IOP Publishing   Phys. Med. Biol. 71 (2026) 015016   https://doi.org/10.1088/1361-6560/ae2db6

Physics in Medicine & Biology

IPEM
Institute of Physics and Engineering in Medicine

Check for updates

OPEN ACCESS

RECEIVED
29 August 2025

REVISED
18 November 2025

ACCEPTED FOR PUBLICATION
16 December 2025

PUBLISHED
30 December 2025

PAPER

Electron spin resonance measurements of radiation-induced radicals under conventional and ultra-high dose rate electron irradiation

Johanna Pehlivan[1,*], **Elke Beyreuther**[2,3], **Felix Horst**[2,4], **Michael J Nasse**[5], **Jörg Pawelke**[2,4], **Dieter Leichtle**[1], **Oliver Jäkel**[6,7] **and Bernhard Holzapfel**[8]

[1] Karlsruhe Institute of Technology (KIT), Institute for Neutron Physics and Reactor Technology, Eggenstein-Leopoldshafen, Germany
[2] OncoRay—National Center for Radiation Research in Oncology, Faculty of Medicine and University Hospital Carl Gustav Carus, Dresden University of Technology (TUD); Helmholtz-Zentrum Dresden-Rossendorf (HZDR), Dresden, Germany
[3] Helmholtz-Zentrum Dresden-Rossendorf (HZDR), Institute of Radiation Physics, Dresden, Germany
[4] Helmholtz-Zentrum Dresden-Rossendorf (HZDR), Institute of Radiooncology-OncoRay, Dresden, Germany
[5] Karlsruhe Institute of Technology (KIT), Institute for Beam Physics and Technology, Eggenstein-Leopoldshafen, Germany
[6] German Cancer Research Center (DKFZ), Division of Medical Physics in Radiation Oncology, Heidelberg, Germany
[7] Heidelberg Ion Beam Therapy Center (HIT) at Heidelberg University Hospital, Heidelberg, Germany
[8] Karlsruhe Institute of Technology (KIT), Institute for Technical Physics, Eggenstein-Leopoldshafen, Germany
[*] Author to whom any correspondence should be addressed.

E-mail: johanna.pehlivan@kit.edu

Keywords: FLASH effect, radical–radical recombination, ESR

Supplementary material for this article is available online

Abstract

Ultra-high dose rate (UHDR) radiotherapy has been shown in preclinical studies to reduce normal tissue toxicity without compromising tumour control, a phenomenon referred to as the Flash effect. The radiochemical and biological mechanisms responsible for this effect remain unclear. This study investigates radical formation and oxygen depletion under UHDR and conventional dose rate (CDR) conditions to gain mechanistic insight. Radical formation was investigated using electron spin resonance (ESR) spectroscopy with both spin trapping and spin probe techniques. Oxygen consumption was monitored continuously during irradiation to complement radical yield measurements. E3 medium containing either spin traps (DMPO, DEPMPO, BMPO) or spin probes (CMH, TMTH, CAT1H) was prepared under hypoxic, physioxic, and normoxic conditions. Irradiations were performed at the Electron Linac for beams with high Brilliance and low Emittance at the Helmholtz-Zentrum Dresden-Rossendorf (HZDR) with 30 MeV electrons across a broad range of dose rates (0.1 $\mathrm{Gy\,s^{-1}}$–10^5 $\mathrm{Gy\,s^{-1}}$). Spin probe measurements enabled consistent comparisons between CDR and UHDR, revealing a significant dependence of spin concentration on both oxygenation and dose rate. In contrast, spin trapping showed reduced radical yields with decreasing oxygen levels, but no significant dose-rate dependence. Direct comparisons between UHDR and CDR were limited by differences in the decay kinetics of the spin adducts. Oxygen measurements confirmed a reduced oxygen consumption at UHDR, with the extent of depletion strongly dependent on initial oxygen concentration. The results support the hypothesis that UHDR conditions promote radical–radical recombination, shifting the reaction equilibrium and reducing the pool of radicals available to react in the homogeneous chemical phase, particularly with oxygen. The combined application of ESR spin trapping, spin probes, and real-time oxygen measurements offers complementary insight into dose-rate-dependent radical processes.

1. Introduction

The potential use of ultra-high dose rates (UHDR) in radiotherapy has gained increasing attention in recent years due to the opportunity it offers to expand the therapeutic window in clinical practice. The so-called Flash effect at UHDR ($>40\,\mathrm{Gy\,s^{-1}}$) has been shown preclinically to significantly reduce normal tissue toxicity while maintaining tumour control comparable to conventional dose rate (CDR) radiotherapy ($\sim 0.1\,\mathrm{Gy\,s^{-1}}$) (Favaudon *et al* 2014). By reducing normal tissue toxicity, it may enable treatments with fewer side effects or allow for dose escalation in tumours that respond poorly to conventional treatment, without increasing the risk of complications compared to current treatment strategies.

The differential Flash effect has been validated in preclinical studies with several animal models and for electron, photon, proton and heavy ion beams. First veterinarian and human clinical trials are currently ongoing. A better understanding of the mechanisms of the Flash effect is fundamental for the optimisation of the parameters triggering the effect and to allow broader clinical translation. Current research aims to address two key questions: first, what causes UHDR irradiation to reduce radiation-induced biological damage; and second, why does this protective effect appear to preferentially affect healthy tissue, while tumour control remains uncompromised (Limoli and Vozenin 2023)?

One of the earliest explanations proposed for the Flash effect was the oxygen depletion hypothesis (Pratx and Kapp 2019). It proposes that, at UHDR, radiation-induced radicals consume oxygen so rapidly that transient hypoxia develops, reducing the oxygen fixation effect and thereby limiting biological damage in normal tissues. This idea appeared plausible because tumours, which are often already hypoxic, would be less affected, potentially explaining the preservation of tumour control. Subsequent work has clearly shown that total oxygen depletion during irradiation decreases with increasing dose rate (Cao *et al* 2021, Jansen *et al* 2022b, Sunnerberg *et al* 2024). These findings contradict the oxygen depletion hypothesis and have shifted attention towards alternative radiochemical mechanisms.

Another hypothesis proposed to explain both the Flash effect and the reduced oxygen consumption observed at UHDR is radical–radical recombination. It suggests that the very short duration of UHDR irradiation transiently generates high concentrations of reactive species, which promotes their mutual recombination and neutralisation before they can react with molecular oxygen (O_2) (Jansen *et al* 2022a). This mechanism provides a potential explanation not only for the dose-rate dependence of oxygen depletion, but also for the Flash effect itself. Faster mutual recombination also limits the lifetime of highly reactive species such as peroxyl ($ROO^\bullet$) and hydroxyl radicals ($OH^\bullet$), thereby reducing their ability to damage critical targets in cells such as DNA (Labarbe *et al* 2020). In well-oxygenated normal tissues, this accelerated radical recombination may help to prevent the accumulation of DNA-damaging species and the fixation of oxidative lesions, ultimately sparing healthy cells. In contrast, in hypoxic tumour environments where oxygen is already scarce, fewer reactive oxygen species (ROS) are produced, so the additional protection under UHDR conditions is likely limited. As a result, the protective effect seen in normal tissues may be reduced or entirely absent in tumours.

This difference parallels the well-established oxygen enhancement effect in radiotherapy, where oxygen stabilises radiation-induced damage and hypoxic tumour regions are inherently more radioresistant. As a consequence, tumour control in anoxic or hypoxic regions requires higher doses, a concept that has been demonstrated in oxygen-guided or boost-dose treatments targeting hypoxic subvolumes (Epel *et al* 2019). Central to this radiochemical effect is the process of water radiolysis: the interaction of ionising radiation with intracellular water leads to the generation of various short-lived reactive species (figure 1). Primary radical species such as $OH^\bullet$, hydrated electrons (e^-_{aq}), and hydrogen atoms ($H^\bullet$, often referred to as the hydrogen radical) are generated within femto- to picoseconds after energy deposition during the physicochemical phase. These species rapidly undergo diffusion-controlled reactions including recombination and oxygen-dependent processes within the first few nanoseconds (Sonntag 2006).

Direct experimental access to oxygen dynamics and radical chemistry is therefore essential to critically test mechanistic hypotheses of the Flash effect. By combining real-time oxygen measurements during irradiation with post-irradiation electron spin resonance (ESR) spectroscopy, we can quantify both the immediate oxygen consumption and the integrated radical yields that underlie dose-rate effects. Spin traps capture primary radicals such as $OH^\bullet$ or e^-_{aq} within nanosecond to microsecond time frames, stabilising them for ESR spectroscopy measurement (Schuler *et al* 1971). In contrast, spin probes, typically present at lower concentrations, react with longer-lived ROS (e.g. $O_2^{\bullet-}$) and therefore reflect broader and often delayed redox changes in a given system (Giamello and Brustolon 2009).

These complementary approaches provide physicochemical insights that form the foundation for interpreting subsequent *in vivo* experiments. By connecting oxygen consumption and radical yields observed in simple systems to biological responses in complex tissues, they help to establish a framework for the rational design of preclinical studies. To facilitate translation towards preclinical models,

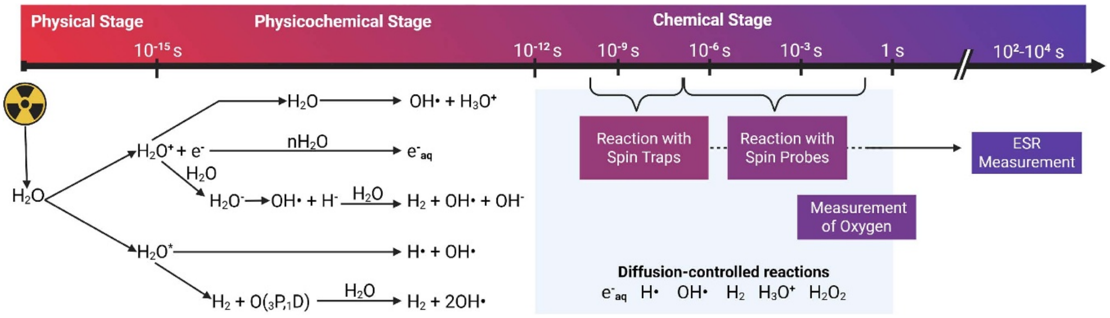

Figure 1. Timeline of water radiolysis (Sonntag 2006) and radical detection. Ionising radiation produces short-lived species on the femtosecond-picosecond timescale. Spin probes detect radicals via oxidation, whereas spin traps form specific paramagnetic adducts (Khan *et al* 2003, Dikalov *et al* 2011). Created in BioRender. Pehlivan J (2026) https:// BioRender.com/7sfvnqb.

our measurements were performed in E3 medium, the standard medium for zebrafish embryos (ZFE) (Brand *et al* 2002). E3, with its ionic composition, offers a chemically more representative medium than water. Starting with this intermediate level of complexity allows us to gradually adapt the methodology for future application in more complex biological systems, such as ZFE or cell cultures.

2. Methods and materials

2.1. Sample preparation and oxygen measurement

Samples were prepared in E3 ZFE medium supplemented with diethylenetriaminepentaacetic acid (DTPA, 25 μM; ThermoFisher Scientific) as a metal chelator. Since E3 medium offers a defined and reproducible composition with a physiologically relevant pH and additional ionic components, making it chemically more representative of *in vivo* environments while still providing experimental stability. For each sample, one of the spin traps or spin probes listed in table 1 was added.

The spin trap DMPO is widely used due to its simple and well-characterised ESR spectra, which facilitates data interpretation. However, it forms relatively short-lived adducts, particularly with superoxide ($O_2^{\bullet -}$) and $OH^{\bullet}$. In contrast, BMPO and DEPMPO form more stable radical adducts and allow better distinction between different ROS species. DEPMPO in particular offers improved stability of $O_2^{\bullet -}$ and $OH^{\bullet}$ adducts, making it well suited for longer measurement times and more complex ROS environments (Bacic *et al* 2008).

While spin traps provide specificity in radical identification, spin probes offer a complementary approach with distinct advantages in biological systems. Unlike spin traps, they do not form adducts with radicals but are directly oxidised by species like $O_2^{\bullet -}$, yielding stable nitroxides detectable by ESR. These reactions proceed efficiently, allowing detection of $O_2^{\bullet -}$ at much lower concentrations (0.05–1 mM) compared to the higher amounts typically required for spin traps (100 mM). This reduces potential cytotoxicity and minimises interference with native redox processes. Furthermore, the single-step reaction with $O_2^{\bullet -}$ and the absence of redox cycling artefacts support their suitability for *in vivo* and cellular applications (Gotham *et al* 2020). Their chemical simplicity, low background, and relative stability make spin probes particularly attractive for systems where time-resolved detection is not feasible, but integrated oxidative changes are of interest (Dikalov *et al* 2011). Spin probes were first dissolved in phosphate-buffered saline (PBS, pH 7.4) before being added to the E3 medium. For experiments conducted at acidic pH (pH 4), spin probes were used without additional buffering, allowing direct comparison between physiological and acidic conditions. The low pH condition was included to explore how protonation affects the chemical behaviour of the probe and its radicals. At low pH, protonation shifts the equilibrium toward neutral probe and radical species, which can alter redox kinetics and increase nitroxide stability (Khramtsov *et al* 2004). The acidic condition (pH $\approx$ 4) was also chosen as an exploratory model representing an extreme, acidified regime that may occur locally in tumour microenvironments. While typical extracellular tumour pH values are only moderately acidic (around 6.5–6.8), transient or compartmental acidification can reach lower values (Hosonuma and Yoshimura 2023). ESR measurements were performed post-irradiation, complementary oxygen measurements were carried out in real time during irradiation (sensor response time: $t_{90} < 0.3$ s) to measure oxygen depletion and support kinetic interpretation of the radical reactions (figure 2).

Samples were prepared for three defined target oxygenation levels: hypoxic (8 mmHg, corresponding to 5 % air saturation), physioxic (38 mmHg, approx. 24 % air saturation), and normoxic (160 mmHg,

Table 1. Spin traps and spin probes used in this study.

Abbreviation	Compound	Concentration	Supplier
Spin traps			
DMPO	5,5-Dimethyl-1-pyrroline-N-oxide	50 mM	Cayman Chemical
BMPO	5-tert-Butoxycarbonyl-5-methyl-1-pyrroline N-oxide	25 mM	Enzo Life Sciences
DEPMPO	5-(Diethoxyphosphoryl)-5-methyl-1-pyrroline N-oxide	25 mM	Enzo Life Sciences
Spin probes			
CAT1H	1-Hydroxy-3-carboxy-2,2,5,5-tetramethylpyrrolidine	100 μM	Noxygen Science Transfer & Diagnostics GmbH
CMH	1-Hydroxy-3-methoxycarbonyl-2,2,5,5-tetramethylpyrrolidine	100 μM	Noxygen Science Transfer & Diagnostics GmbH
TMTH	1-Hydroxy-4-[2-(triphenylphosphonio)acetamido]-2,2,6,6-tetramethylpiperidine	100 μM	Noxygen Science Transfer & Diagnostics GmbH

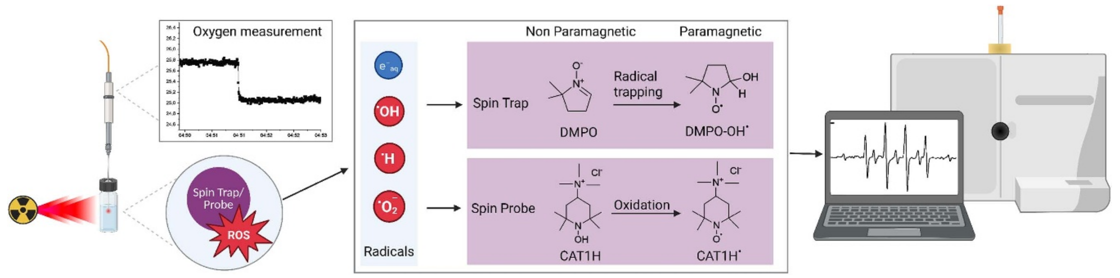

Figure 2. Schematic overview of the experimental setup and spin-based radical detection. Irradiated samples containing spin traps or spin probes were analysed by ESR spectroscopy. Oxygen levels were monitored in real time during irradiation using a fibre-optic sensor. Spin traps (e.g. DMPO) form stable paramagnetic adducts upon reacting with short-lived radicals (e.g. $OH^{\bullet}$), whereas spin probes (e.g. CAT1H) are directly oxidised by ROS to form detectable nitroxide radicals. ESR measurements were performed after irradiation. Created in BioRender. Pehlivan (2026) https://BioRender.com/ vgss8he.

equivalent to 100 % air saturation). Hypoxic and physioxic conditions were established using a hypoxia chamber (HypoxyLab, Oxford Optronix, UK), while normoxic samples were prepared separately under ambient air conditions. Oxygen concentrations in the sample prior to irradiation were confirmed using a fibre-optic oxygen sensor (Model NX-BF, used with OxyLite oxygen monitor, Oxford Optronix, UK). Due to experimental variability in oxygen equilibration, samples did not always precisely reach the intended target oxygen levels. For grouped data presentation, samples were therefore classified based on their measured initial oxygen concentrations. Specifically, values $\leqslant 10\%$ air saturation were considered hypoxic, values between $\geq 10\%$ and $\leqslant 70\%$ as physioxic, and values $> 70\%$ as normoxic.

For a subset of samples, oxygen levels were continuously monitored during irradiation using a fibre-optic oxygen microsensor (OXR50-UHS, PyroScience GmbH, Germany), which was inserted through a septum into the sealed sample prior to irradiation. The sensor output of the Pyroscience system was recorded in units of % air saturation, where 100% corresponds to the equilibrium oxygen concentration of air-equilibrated medium under ambient pressure and room temperature (approximately 21% O_2 in air). Thus, measured values ranged from 0% (fully deoxygenated) to 100% air saturation. Representative real-time oxygen traces at CDR and UHDR are provided in the Supplement (figure S1). To increase the number of data points on oxygen depletion in different initial oxygen concentrations, some continuously monitored samples were irradiated multiple times at varying dose rates. A minimum delay of 30 s between irradiations ensured the decay of short-lived radiolytic species.

2.2. Irradiation and dosimetry

Irradiations were performed at the superconducting research Electron Linac for beams with high Brilliance and low Emittance (ELBE) at the Helmholtz-Zentrum Dresden-Rossendorf (HZDR) (Gabriel *et al* 2000) using a 30 MeV electron beam in two distinct dose-rate regimes (table 2). Electron bunches of 5 ps bunch length were delivered quasi-continuously at 13 MHz frequency, but differed in bunch

Table 2. Dose-rate regimes used for irradiation with 30 MeV electrons at the ELBE accelerator. Total dose is given as mean ± standard deviation for all sample irradiations.

Regime	Mean dose rate	Bunch dose rate	Total dose [Gy]
CDR—Conventional dose rate	$\sim 0.1\,\mathrm{Gy\,s^{-1}}$	$\sim 10^3\,\mathrm{Gy\,s^{-1}}$	30.0 ± 0.1
UHDR—Ultra-high dose rate	$\sim 10^5\,\mathrm{Gy\,s^{-1}}$	$\sim 10^9\,\mathrm{Gy\,s^{-1}}$	29.8 ± 0.2

charge (dose) by several orders of magnitude resulting in different dose rates and therefore different irradiation durations for the same total dose. A previously established irradiation and dosimetry setup (Pawelke *et al* 2021, Karsch *et al* 2022, Horst *et al* 2024) was complemented by a newly available flash-Diamond detector (fD) as an additional dose measurement device at UHDR. A detailed overview of all detectors and readout devices used in the dosimetric setup is provided in table S1 (see Supplementary Materials). Following the vacuum exit window, the ELBE electron pencil beam is broadened by a 2 mm thick polymethyl methacrylate (PMMA) scatterer to achieve a homogeneous lateral dose distribution (+/− 5%) of 8 mm diameter at sample position. In short distance, an integrating current transformer followed by a transmission ionisation chamber (T-IC) at beam exit are used for constant monitoring of the bunch charge and dose delivery. Downstream, either the sample holder can be placed on beam axis using a remote controlled linear axis or an Advanced Markus ionisation chamber (M-IC) equipped with a build-up cap (1 mm thick PMMA) and a fD can be moved to sample position for dosimetry and for setting up the beam parameters across the different dose-rate regimes. Radiochromic dosimetry films, either type GAFchromic EBT3 or EBT-XD were attached directly in front of each sample. A phosphorescence screen (Lanex Screen) was used prior to sample irradiations for real-time verification of beam position and lateral beam profile, particularly after beam interruptions, in particular for entering the irradiation cave for sample change. These checks were performed without any samples in the beam path to avoid scattering effects and to ensure that the beam was properly centred before irradiation. Minor beam drifts were corrected accordingly. For practical reasons, the Lanex screen was positioned several centimetres downstream of the sample plane, thus, it provided relative beam information rather than the exact fluence at the sample position. During the actual sample irradiations, radiochromic films were placed immediately in front of each sample to record the 2D spatial dose distribution at the sample position. Film readout was performed retrospectively, providing a sample-specific verification of dose delivery and homogeneity across different dose-rate regimes. To verify the consistency of the previously established dosimetric setup and to exclude potential drifts or anomalies during irradiation, the dose delivery is monitored online using the T-IC, cross-calibrated to fD absorbed-dose-to-water readout at sample position. The fD sensitivity was determined for 20 MeV electrons at the Physikalisch-Technische Bundesanstalt (PTB, Braunschweig, Germany) (Subiel *et al* 2024). As shown by Bourgoin *et al* (2022), Kranzer *et al* (2022), the detector response is dose-rate independent up to $5 \times 10^6\,\mathrm{Gy\,s^{-1}}$ by validating a linear response to single pulses (below 4 μs duration) of up to more than 20 Gy per pulse. Since the T-IC readout was influenced by strong recombination effects at UHDR, cross calibration has been performed individually for each dose-rate group on a daily basis. Independent cross calibration was performed with the M-IC, calibrated for $^{60}\mathrm{Co}\ \gamma$ dose readout, at sample position. For this, the chamber readout was corrected for air density, radiation quality of 30 MeV electrons ($k_{\mathrm{E}} = 0.88$) and dose rate dependent recombination effects. The end of irradiation took place after reaching the previously determined T-IC readout value (CDR) or number of bunches (UHDR).

To ensure consistency across irradiations, radiochromic films were placed with each sample to verify relative dose within each dose-rate group. These films are not strictly dose-rate independent (Villoing *et al* 2022), yet they remain suitable for internal consistency verification. For calibration, EBT3 films were referenced to 21 MeV electron doses measured at a clinical linac (type Oncor Impression, Siemens AG, Erlangen, Germany) and EBT-XD films to 18 MeV electron doses measured at another clinical linac (type TrueBeam, Varian Medical Systems, Palo Alto, CA, USA). In addition to the two main dose rate categories (CDR and UHDR), several intermediate dose rates (ranging from $10\,\mathrm{Gy\,s^{-1}}$ to $1000\,\mathrm{Gy\,s^{-1}}$) were also tested to explore potential dose rate dependencies across a broader range. However, for grouped statistical analyses and visualisation, dose rates were categorised as either CDR ($\leqslant 00.25\,\mathrm{Gy\,s^{-1}}$) or UHDR ($\geqslant 40\,\mathrm{Gy\,s^{-1}}$), based on literature thresholds used in Flash radiobiology (Favaudon *et al* 2014). This study specifically focused on the highest achievable dose rates, as these conditions maximise instantaneous radical concentrations and thus the likelihood of radical–radical interactions. The extent to which these effects persist under clinically relevant dose-rate and pulse-structure conditions remains to be clarified. All samples received a total dose of 30 Gy, chosen based on its suitability for future endpoint studies in ZFE, which are planned as a follow-up to the present experiment. For all dose-normalised data, an overall standard dosimetry uncertainty of 5% was assumed. This includes the uncertainty associated with the traceable sensitivity determination of the reference fD at PTB (≈3%) (Subiel *et al* 2024), daily cross-calibration of the T-IC and potential variations between the irradiation sessions (≈2%), and positioning/setup reproducibility effects (<1%). Minor contributions (≈1%) from environmental corrections and long-term detector stability are considered to be covered by the conservative rounding to a total uncertainty of 5%.

2.3. Electron spin resonance measurement

ESR measurements were conducted using a Magnettech ESR5000 spectrometer (Bruker, Germany). All samples were measured at room temperature in 50 μl capillaries (Hirschmann Ringcaps). ESR spectra were recorded at X-band (9.4 GHz) with a modulation frequency of 100 kHz, modulation amplitude of 0.1 mT, and a sweep time of 12 s. The sweep range and microwave power were adjusted for each spin trap/probe based on previous measurements of the saturation profile to ensure operation in the linear response range (table S2 in the Supplementary Materials). For samples containing spin traps (DMPO, DEPMPO, BMPO), measurements were performed approximately 5 min post-irradiation to ensure comparability of the data, given the known instability of spin adducts and considering the time needed after end of irradiation to pickup the sample and prepare for measurement. For samples containing spin probes (CMH, TMTH, CAT1H), the time elapsed after the end of irradiation before measurement was not fixed, due to the higher stability of these compounds in water. To control for potential autoxidation, non-irradiated blank samples were included for all spin probe conditions and were processed identically to the irradiated samples.

Spectral analysis and deconvolution were performed using SpinFit Liquid software (Bruker, Germany). The fitting procedure corrected for baseline drift and background signals and enabled the resolution of overlapping spectral components, allowing quantification of individual radical adducts in spin trap samples. Absolute radical concentrations (M) were obtained from the double-integrated ESR signal intensity using the instrument's internal spin-count calibration. This calibration relates the integrated signal area to the number of spins within the resonator volume under defined spectrometer settings. The resulting spin number was converted to concentration by normalising to the sample volume, assuming linear detector response at the applied microwave power. Component assignments for spin trap spectra were based on literature-reported spectral parameters (Frejaville *et al* 1995, Bruker BioSpin 2022), which served as initial estimates for the fitting routine. The final fitted signal parameters derived from our measurements are summarised in table S3 (Supplementary Materials).

2.4. Data processing and statistical analysis

Oxygen concentration was continuously measured for some samples. Oxygen depletion per unit dose ($\Delta c(\mathrm{O}_2)/D$) was calculated from the difference in mean oxygen concentration between the plateau regions directly before ($c(\mathrm{O}_2)_{\mathrm{initial}}$) and after irradiation ($c(\mathrm{O}_2)_{\mathrm{end}}$), divided by the applied dose (D). The averaging interval was set to 20 s (see Supplementary figure S1). Samples that showed an unexpected increase in oxygen concentration, suggesting air ingress, were excluded from the analysis. The relationship between initial oxygen concentration and oxygen depletion per unit dose was analysed by nonlinear regression using OriginPro 2023 (OriginLab Corporation, Northampton, MA, USA). Data were fitted using the Michaelis–Menten equation, which was previously applied to describe oxygen depletion at varying initial oxygen levels by Jansen *et al* (2022a) (equation (1)). While the Michaelis–Menten model originates from enzyme kinetics, where a specific substrate binds to an enzyme, it can be used more generally to describe processes with a saturating dependence on reactant availability. In our analysis, the initial oxygen concentration ($c(\mathrm{O}_2)_{\mathrm{initial}}$) is used in place of the substrate concentration.

To represent conditions at UHDR and high oxygen concentrations, the Michaelis–Menten model was extended by an exponential modulation term (equation (2)). This term allows the reaction rate to deviate from pure Michaelis–Menten saturation at high initial oxygen concentrations, capturing potential efficiency losses in oxygen-dependent pathways under elevated radical densities. The parameter α quantifies this modulation, representing dose-rate-dependent effects such as radical–radical recombination and diffusion limitations that become relevant at high concentrations of ROS. It should be noted that equation (2) does not include dose rate as an explicit variable; instead, dose-rate effects are embedded in the empirical parameter α, which serves as an effective descriptor of the observed dependence.

$$\frac{\Delta c(\mathrm{O}_2)}{D} = \frac{\Delta c(\mathrm{O}_2)_{\max} \cdot c(\mathrm{O}_2)_{\mathrm{initial}}}{K_{\mathrm{M}} + c(\mathrm{O}_2)_{\mathrm{initial}}} \tag{1}$$

$$\frac{\Delta c(\mathrm{O}_2)}{D} = \frac{\Delta c(\mathrm{O}_2)_{\max} \cdot c(\mathrm{O}_2)_{\mathrm{initial}}}{K_{\mathrm{M}} + c(\mathrm{O}_2)_{\mathrm{initial}}} \cdot \exp\left(-\alpha \cdot c(\mathrm{O}_2)_{\mathrm{initial}}\right) \tag{2}$$

where:

$\Delta c(\mathrm{O}_2)$	change in oxygen concentration during irradiation [% air saturation]
D	applied dose [Gy]
$c(\mathrm{O}_2)_{\mathrm{initial}}$	initial oxygen concentration [% air saturation]
$\Delta c(\mathrm{O}_2)_{\mathrm{max}}$	maximum oxygen depletion (saturation value) [% air saturation]
K_{M}	Michaelis–Menten constant, oxygen concentration at which the depletion rate reaches half of its maximum [% air saturation]
α	parameter quantifying dose-rate-dependent efficiency losses in oxygen consumption caused by elevated ROS densities

Models were compared using Akaike's information criterion (AIC), which trades off goodness of fit against model complexity. Fit quality was summarised by the adjusted coefficient of determination (R^2_{adj}). Parameter estimation was performed by nonlinear least squares (Levenberg–Marquardt algorithm), and uncertainties were derived from the covariance matrix.

Due to slight variations in measurement start times for the ESR spin trap measurements and the known instability of the spin adducts, all data sets were truncated and aligned so that the average recording time fell within a common 2 min window. No kinetic decay correction was applied, as decay behaviour is likely influenced by key experimental parameters such as oxygen concentration and dose rate, variables that were central to this study. Applying a uniform decay model across all conditions could therefore not only introduce additional uncertainty but might also obscure real, condition-dependent differences in radical behaviour.

Quantification of spin probe ESR signals was based on the spin concentrations obtained from spectral fitting. Prior to dose normalisation, the signal of the corresponding non-irradiated blank was subtracted to correct for the known effect of autoxidation, which occurs even without irradiation due to ambient oxygen.

To assess the effects of initial oxygen concentration and dose rate on dose-normalised spin adduct concentrations, a two-way analysis of variance (ANOVA) was performed. This analysis allowed us to test for main effects and interaction effects of the two independent variables. In cases where the ANOVA yielded significant results, Tukey's honest significant difference (HSD) test was used for post-hoc pairwise comparisons. A significance level of $p < 0.05$ was applied for all statistical tests.

3. Results and discussion

3.1. Oxygen depletion as a function of initial oxygen-concentration and mean dose rate

We investigated oxygen depletion during irradiation under varying initial oxygen concentrations and dose rates, with a particular focus on UHDR conditions. The aim was to evaluate whether the previously observed reduction in oxygen consumption at UHDR (Cao *et al* 2021, Jansen *et al* 2022b, Sunnerberg *et al* 2024) could be attributed to radical–radical recombination occurring prior to the reaction of free radicals with O_2. The resulting oxygen depletion per unit dose ($\Delta c(\mathrm{O}_2)/D$) was plotted as a function of initial oxygen saturation and mean dose rate for samples containing spin traps (figures 3(a) and (b)) as well as for samples with spin probes (figures 4(a) and (b)) together with additive-free E3 medium. Overall, UHDR irradiation led to significantly lower oxygen depletion than CDR, with the extent of depletion also dependent on the initial oxygen concentration. These findings align with previous reports of reduced oxygen depletion at UHDR *in vitro* (Cao *et al* 2021, El Khatib *et al* 2022, Jansen *et al* 2022a, 2022b) and *in vivo* (Sunnerberg *et al* 2024).

As described in the Methods section, the experimental data were fitted using the mechanistic Michaelis–Menten model (equation (1)). Overall, the model performs well across all groups at low oxygen concentrations and under CDR conditions, where diffusion and radical recombination play a minor role. Notably, a plateau in oxygen depletion becomes apparent at about 20% air saturation, corresponding to roughly 4.2% partial pressure of oxygen (pO_2). This is in good agreement with measurements by Jansen *et al* (2022a) and simulation results by Boscolo *et al* (2020), who report saturation of oxygen consumption beyond 5% pO_2 due to complete scavenging of $\mathrm{e}^-_{\mathrm{aq}}$. However, in E3 medium and spin probe samples, we observed a clear decrease in oxygen depletion per dose at initial normoxic concentrations under UHDR conditions. To quantitatively compare the model performance under CDR and UHDR conditions, AIC values were calculated for both regimes (table S3 in the Supplementary Materials). For the spin probe data, the extended model (equation (2), MM + UHDR) yielded substantially lower AIC and Bayesian Information Criterion (BIC) values under UHDR irradiation ($\Delta\mathrm{AIC} \approx 16$, Akaike weight > 0.99), indicating decisive support for the inclusion of the exponential correction term. At CDRs, the

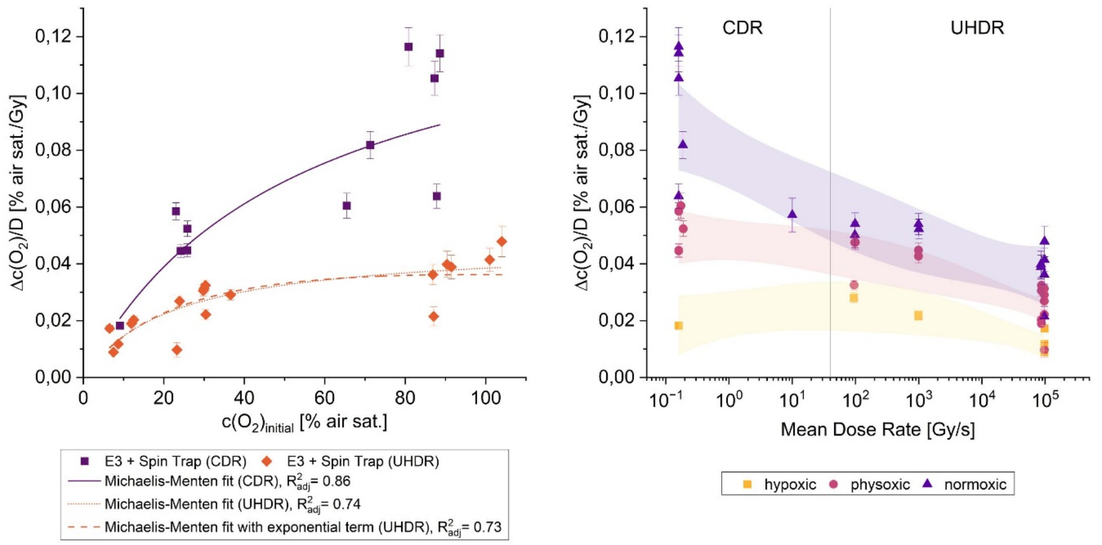

(a) Spin traps in E3 medium: dependence on initial O_2 concentration.

(b) Spin traps in E3 medium: dependence on mean dose rate. Shaded 95 % confidence bands from polynomial fits are shown to guide the eye.

Figure 3. Oxygen depletion per dose ($\Delta c(O_2)/D$) for samples containing spin traps as a function of (a) initial oxygen concentration and (b) mean dose rate. Solid lines in (a) show fits using the Michaelis–Menten model; the dashed line represents the extended model including an exponential correction term for radical recombination.

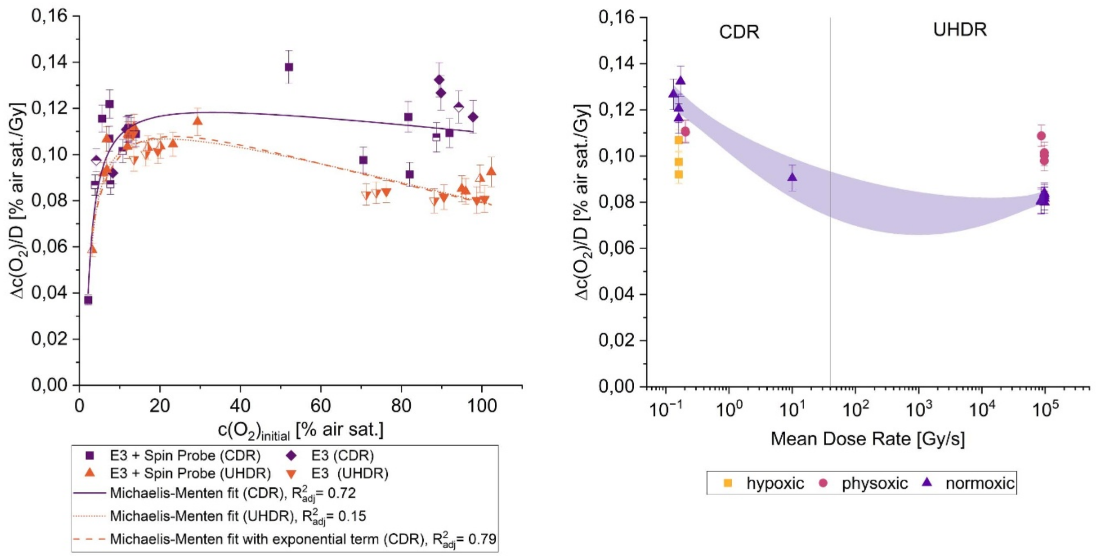

(a) Spin probes in E3 medium (squares) and additive-free E3 medium (diamonds): dependence on initial O_2 concentration. Half-filled symbols indicate samples that were irradiated multiple times.

(b) Data for additive-free E3 medium (without spin probe), dependence on mean dose rate. Shaded 95 % confidence bands from polynomial fits are shown to guide the eye.

Figure 4. Oxygen depletion per dose ($\Delta c(O_2)/D$) for samples containing spin probes as a function of (a) initial oxygen concentration and (b) mean dose rate. Solid lines in (a) show fits using the Michaelis–Menten model; the dashed line represents the extended model including an exponential correction term for radical recombination. The model fits were obtained from the combined data set (spin probe and E3 + E3).

improvement was minor ($\Delta\mathrm{AIC} \approx 4$), suggesting only a weak non-ideality rather than an explicit dose-rate dependence. For the spin trap data, the classical model remained sufficient across both regimes, consistent with the absence of saturation. While equation (2) provides a good overall description of the data, the intermediate oxygen range is represented by fewer data points, which naturally increases the uncertainty of the fitted curvature in this region. Under UHDR irradiation, high local radical densities promote radical–radical reactions and interactions with competing solutes, reducing the fraction that reacts with O_2 (Jansen *et al* 2022a). Once oxygen-dependent pathways are saturated, further increases in pO_2 do not lead to higher oxygen consumption. Instead, diffusion limitations and the build-up of secondary species such as $O_2^{\bullet-}$ and $HO_2^{\bullet}$ can kinetically limit further oxygen engagement, causing depletion per dose to saturate or even decline despite greater oxygen availability. The presence of a spin trap led to a notable reduction in oxygen depletion. The effect varied with oxygen concentration, being most pronounced under hypoxic and physoxic conditions. Despite this, the overall dependence of oxygen consumption on dose rate and initial oxygen concentration remained evident in spin trap-containing samples (figure 3(a)).

Given that spin traps compete with oxygen and other solutes for radical reactions, and can alter the balance between radical recombination and oxygen-dependent pathways, their use introduces a controlled yet non-negligible perturbation of the system. Nevertheless, this disturbance of the native redox kinetics constitutes a methodological limitation that should be considered when comparing to additive-free conditions. Spin traps such as DMPO, DEPMPO, and BMPO act as radical scavengers by intercepting short-lived species like $OH^{\bullet}$, e_{aq}^- and $H^{\bullet}$ (table 4). In doing so, they compete with O_2 and other solutes for reaction with free radicals, thereby influencing the overall reaction network. Despite the presence of spin traps in high concentrations, oxygen consumption persisted, indicating that fast-reacting species such as e_{aq}^- and $H^{\bullet}$ can still react with O_2 before encountering a spin trap. This is particularly notable given that spin traps were present in high concentrations (25–50 mM), vastly exceeding the dissolved oxygen levels under 100% air-saturated conditions (~0.2mM). However, because the bimolecular rate constants k for the reactions of e_{aq}^- and $H^{\bullet}$ with O_2 are on the order of $10^{10}\,M^{-1}\,s^{-1}$ (see table 4), oxygen effectively outcompetes spin traps, whose rate constants are several orders of magnitude lower (10^6–$10^9\,M^{-1}\,s^{-1}$) for these species.

Samples containing spin probes such as CMH, TMTH, or CAT1H exhibited oxygen depletion levels comparable to those in additive-free controls. While these spin probes undergo one-electron oxidation by reactive species and form stable nitroxides detectable by ESR, they do not trap radicals in the classical sense. Acting as competing substrates, spin probes can intercept a fraction of the radicals, but they are typically used at low concentrations (100 μM) and react selectively with only certain species ($OH^{\bullet}$ or $O_2^{\bullet-}$ but typically not with e_{aq}^- (table 4)). Consequently, they do not substantially affect the overall balance of early radiolysis reactions. In particular, they do not meaningfully interfere with oxygen consumption processes immediately following irradiation.

3.2. ESR-based quantification of radical species using spin traps

The use of the spin traps DMPO, DEPMPO and BMPO in ESR measurements enabled the differentiation of radical species based on their characteristic spectral features (figure 5(a)). Measurements with BMPO and DEPMPO were performed only for a limited number of conditions, in some cases without replicates. These results are therefore interpreted in a qualitative manner and serve primarily to illustrate the applicability of the method to different spin traps. The measured spectra showed a predominant formation of $OH^{\bullet}$ adducts, with additional contributions from $H^{\bullet}$.

The fitted spectra closely matched the measured data, enabling quantification of individual radical species. Examples of both fitted spectra and the spectral components of the radical adducts are given in supplementary figures S2–S4.

For consistency, all three spin-trap datasets were included in the two-way ANOVA framework described below. However, the BMPO and DEPMPO data were treated in an exploratory manner due to their limited sample size and deviations from variance homogeneity. The corresponding results are reported for completeness and should be regarded as indicative rather than confirmatory. Spin adduct concentrations were normalised to the applied dose. $OH^{\bullet}$ and $H^{\bullet}$ adducts were evaluated separately to account for their differing chemical reactivity and stability. The results of analysis of the influence of the initial oxygen concentration and dose rate on the radical yield are shown in figure 6.

For all three spin traps, $OH^{\bullet}$ adduct yields were highest under normoxic conditions. Two-way ANOVA revealed a significant effect of initial oxygen level on the concentration of $OH^{\bullet}$ adducts formed with DMPO ($p < 0.0001$) and BMPO ($p < 0.0001$), whereas no significant effect was observed for DEPMPO ($p = 0.145$). Post-hoc comparisons showed that adduct concentrations were significantly higher under normoxic conditions than under both hypoxic and physioxic conditions. No significant difference was found between hypoxic and physioxic groups for DMPO-OH, while BMPO-OH showed a significant difference ($p = 0.003$) between these two conditions.

The observed increase in $OH^{\bullet}$ adduct yield under normoxic conditions is consistent with Monte Carlo simulations by Boscolo *et al* (2020), who report slightly elevated $OH^{\bullet}$ yields at higher initial O_2

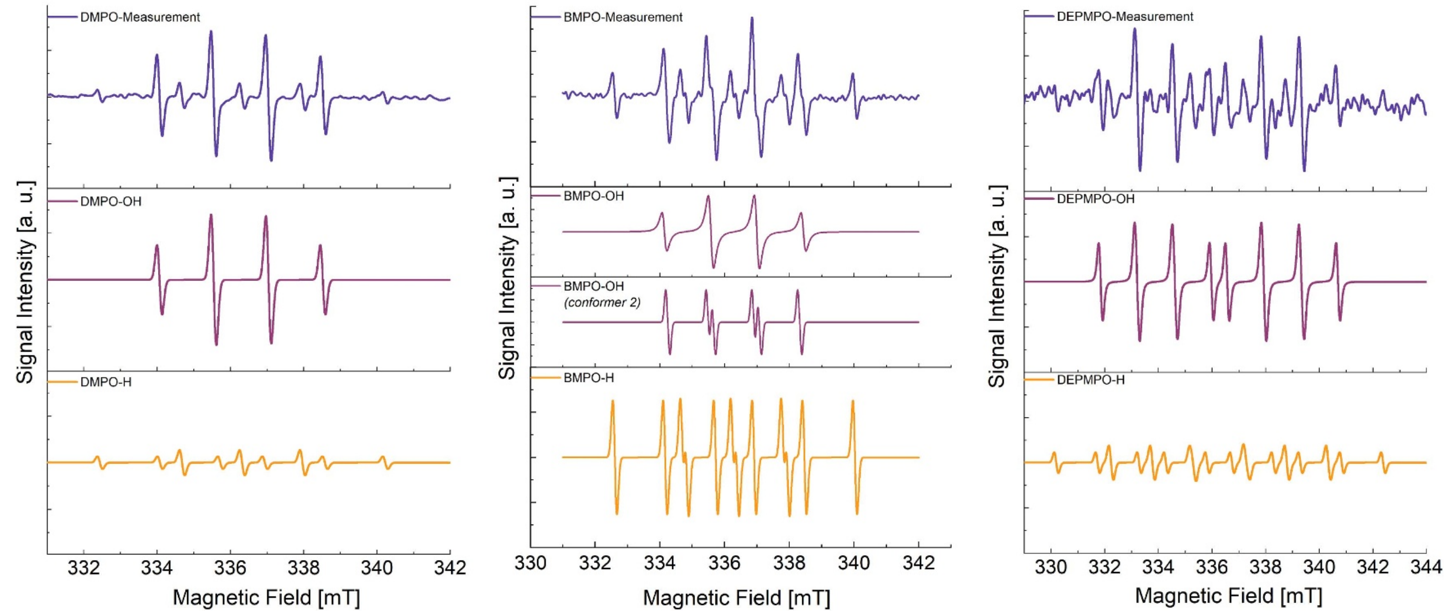

(a)

(b)

Figure 5. Representative ESR spectra of DMPO (a), BMPO (b), and DEPMPO (c) samples. Experimental spectra (top traces) are shown together with the simulated component fits for hydroxyl ($OH^{\bullet}$) and hydrogen ($H^{\bullet}$) adducts obtained from SpinFit modelling. The individual component traces illustrate the relative contributions of $OH^{\bullet}$ and $H^{\bullet}$ species to the measured composite spectra. For BMPO, two $OH^{\bullet}$ components are displayed, corresponding to distinct conformers of the BMPO-OH adduct.

Table 3. ANOVA p-values for spin trap experiments. Significant results ($p < 0.05$) are shown in bold. Columns correspond to initial oxygen concentration ($O_{2,\mathrm{initial}}$), mean dose rate (Mean DR), and their interaction ($O_{2,\mathrm{initial}} \times$ DR). Significant main effects for $O_{2,\mathrm{initial}}$ were further analysed using Tukey's HSD post-hoc tests (see table S7 in the Supplementary Materials).

Spin trap	$O_{2,\mathrm{initial}}$	Mean DR	$O_{2,\mathrm{initial}} \times$ Mean DR
DMPO-OH	$\boldsymbol{p < 0.001}$	$p = 0.605$	$p = 0.973$
DMPO-H	$p = 0.165$	$p = 0.3255$	$p = 0.173$
BMPO-OH	$\boldsymbol{p < 0.001}$	$p = 0.142$	$p = 0.101$
BMPO-H	$p = 0.940$	$p = 0.697$	$p = 0.154$
DEPMPO-OH	$p = 0.145$	$p = 0.695$	$p = 0.962$
DEPMPO-H	$p = 0.258$	$p = 0.908$	$p = 0.607$

levels for low LET (linear energy transfer) radiation. This effect can be explained by the fact that dissolved oxygen scavenges solvated electrons, which prevents them from reacting with $OH^\bullet$ radicals. As a result, more $OH^\bullet$ radicals remain available and can be detected.

No statistically significant effect of dose rate on $OH^\bullet$ radical adduct formation was observed for any of the spin traps in the two-way ANOVA. Also no significant interaction between oxygen level and dose rate was observed for any of the spin traps (table 3).

Figures 6(d)–(f) show the dose-normalised concentrations of $H^\bullet$ adducts (DMPO-H, BMPO-H, and DEPMPO-H) formed under varying oxygenation levels and dose rates. Although two-way ANOVA did not reveal statistically significant effects of oxygen concentration or dose rate on $H^\bullet$ adduct formation, a visual inspection of the data suggests a potential trend toward higher yields under normoxic conditions, particularly for BMPO and DEPMPO. However, the observed differences remain small and inconsistent across all conditions and spin traps. In particular, DMPO-H did not show a clear trend, and inter-sample variability was high for BMPO and DEPMPO.

All three traps produced $OH^\bullet$ and $H^\bullet$-derived adducts, with DEPMPO producing the highest overall spin concentrations, followed by BMPO, despite the fact that both were used in lower concentrations of 25 mM, compared to 50 mM for DMPO. The relatively low concentrations of DMPO-H adducts, compared to DEPMPO-H and BMPO-H, may reflect either lower trapping efficiency or increased degradation of DMPO-derived adducts under the experimental conditions. Although direct rate constants for the reactions of DEPMPO and BMPO with e^-_{aq} and $H^\bullet$ are not widely reported, the formation of the corresponding $H^\bullet$ adducts has been experimentally confirmed and their enhanced spin adduct stability relative to DMPO is well documented (Hawkins and Davies 2014). Table 4 summarises key reaction rate constants and adduct stabilities for radicals generated during water radiolysis, based on data from the literature.

In addition to differences in trapping efficiency and adduct stability, the irradiation regime itself can introduce kinetic artefacts that complicate direct comparisons of absolute spin adduct yields. Madden and Taniguchi (2001) showed that under continuous ^{60}Co γ-irradiation (223 Gy min^{-1}) in N_2-saturated DMPO solutions, the DMPO-H spin adduct accumulates over the first ~50 s until formation and decay rates equilibrate. This build-up leads to a rapid cross-reaction with coexisting DMPO-OH, lowering the apparent $OH^\bullet$ adduct yield from the ~94% observed in pulsed electron radiolysis (Madden and Taniguchi 1996) to about 44%.

The effect of systematic artefacts becomes especially relevant when comparing continuous (CDR) and pulsed (UHDR) irradiation regimes in our experiment. While the same dose should in principle generate the same total number of primary radicals, in UHDR all radicals are produced within milliseconds to seconds, whereas at CDR the dose is delivered over minutes. This prolonged delivery allows radical formation and decay to occur concurrently, potentially establishing a dynamic steady state. As ESR records only the time-integrated accumulation of stable adducts, the interplay between radical generation and decay becomes critical. According to radical–radical hypothesis, the shorter generation time in UHDR should reduce the number of radicals available for spin trapping. In CDR, however, ongoing radical decay during irradiation likewise lowers the detectable concentration and can mask true dose-rate-dependent differences in ESR-derived yields, likely contributing to the absence of clear dose-rate trends in our results.

Despite their mechanistic utility, spin traps present notable limitations that restrict their broader application, particularly in biological contexts. High concentrations are often required in the range of 25 to 100 mM to achieve sufficient trapping efficiency, given the short useful life time and low steady-state concentrations of free radicals. However, such concentrations are not biologically neutral. Spin traps may exert cytotoxic effects, disrupt endogenous redox signaling (Khan *et al* 2003). Moreover, the ESR

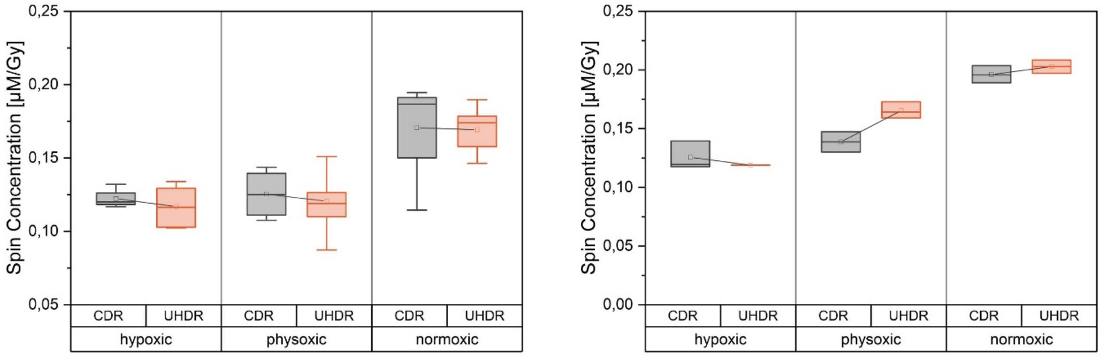

(a) DMPO-OH (b) BMPO-OH

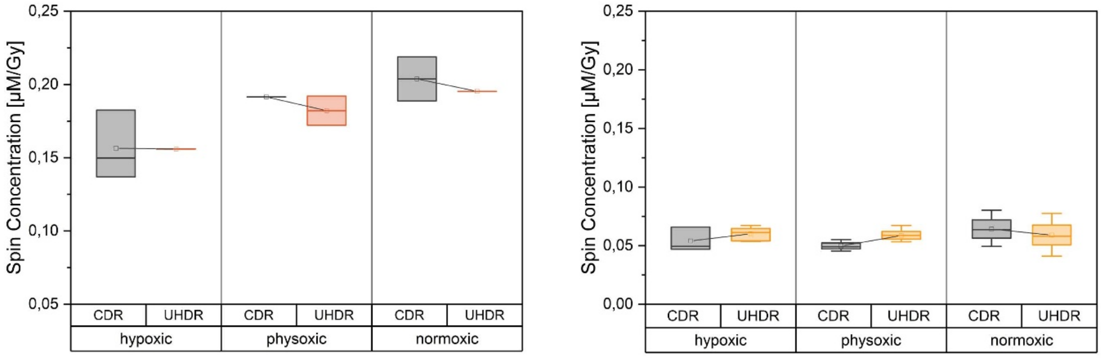

(c) DEPMPO-OH (d) DMPO-H

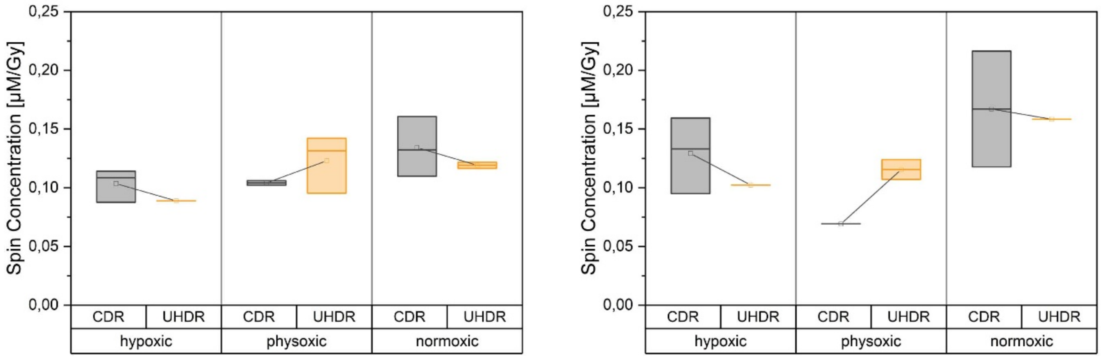

(e) BMPO-H (f) DEPMPO-H

Figure 6. Box plots of dose-normalised spin adduct concentrations under varying oxygenation conditions (hypoxic, physioxic, normoxic) and dose rates (CDR, UHDR) for three different spin traps. Subfigures (a)–(c) show results for the $OH^{\bullet}$ and subfigures (d)–(f) $H^{\bullet}$ adducts of each spin trap. Box plots represent median (horizontal line), interquartile range (box), and total spread (whiskers) per condition. Orange colour denotes UHDR, while grey represents CDR conditions. Replicate counts per condition are listed in table S5 (supplementary materials). Differences in whisker length reflect both experimental variability and unequal sample sizes.

detection of spin adducts inherently reflects the cumulative outcome of multiple competing processes: formation, degradation, and secondary reactions. It is not a direct measure of primary radical yields. In water-based *in vitro* systems, this limitation is manageable, but even here, as discussed above, kinetic artefacts and time-dependent losses may obscure dose rate dependent effects. These challenges are amplified in more complex matrices, where diffusion barriers, antioxidant activity, and variable oxygenation further distort the relationship between radical generation and measured adduct levels. While spin traps provide valuable insights into general trends and mechanistic dependencies, they are difficult to use for precise, quantitative comparisons of radical yields across dose rates or oxygenation levels, particularly in biologically relevant models.

Table 4. Reactivity of spin traps and spin probes with major water-radiolysis radicals.

Compound	Target radical	k ($M^{-1}s^{-1}$)	pH	Adduct $t_{1/2}$
Spin traps				
DMPO	$OH^\bullet$	2.8×10^9 [a]	6.5 [b]	2.9 min [b]
	$H^\bullet$	3.8×10^9 [c]	—	111 s [b]
	e_{aq}^-	2.0×10^{10} [d]	11.0 [d]	—
	$O_2^{\bullet-}$	10 [e]	≥ 7.8 [e]	59 s [e]
	$OOH^\bullet$	6.6×10^3 [e]	5 [e]	—
DEPMPO	$OH^\bullet$	7.8×10^9 [f]	7.4 [b]	22.3 min [b]
	$O_2^{\bullet-}$	~ 90 [f]	7.0 [f]	890 s [f]
BMPO	$OH^\bullet$	2.5×10^9 [g]	7.4 [h]	30 min [h]
	$O_2^{\bullet-}$	<3 [g]	7.4 [i]	23 min [i]
Spin probes				
CMH	$O_2^{\bullet-}$	1.2×10^4 [j]	7.4 [j]	4 h [l]
CAT1H	$O_2^{\bullet-}$	6.4×10^3 [j]	7.4 [j]	4 h [l]
TMTH	$O_2^{\bullet-}$	4.9×10^3 [j]	7.4 [j]	4 h [l]
Reference reactions with oxygen				
O_2	e_{aq}^-	1.9×10^{10} [k]	7.0 [k]	
O_2	$H^\bullet$	2.1×10^{10} [k]	7.0 [k]	

[a] Madden and Taniguchi (2001).
[b] Khan *et al* (2003).
[c] Finkelstein *et al* (1980).
[d] Faraggi *et al* (1984).
[e] Giamello and Brustolon (2009).
[f] Frejaville *et al* (1995).
[g] Goldstein *et al* (2004).
[h] Biller *et al* (2015).
[i] Bruker BioSpin (2022).
[j] Dikalov *et al* (2011).
[k] Buxton *et al* (1988).
[l] Adduct half-life provided by manufacturer (CMH 2025) (biological environment).

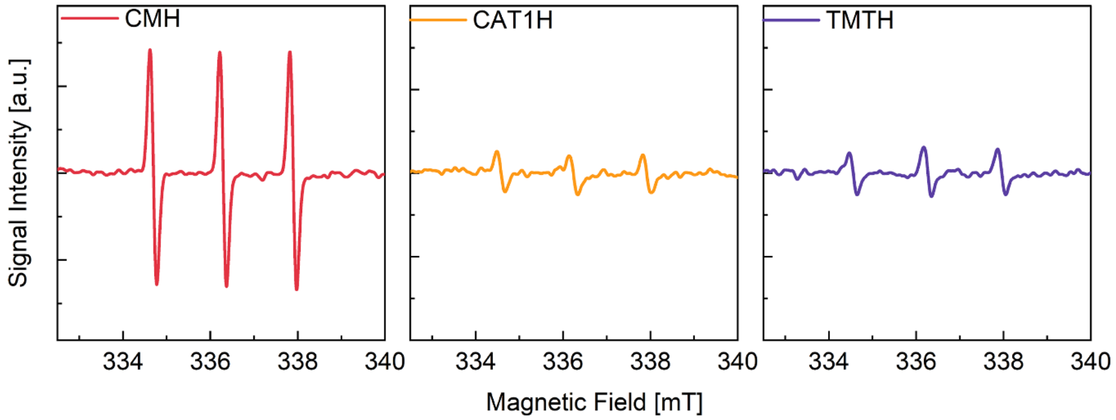

Figure 7. Representative ESR spectra of CMH (right), CAT1H (middle), and TMTH (left) obtained after UHDR irradiation at approximately 24% air saturation, corresponding to physioxic oxygen levels. The spectra shown have not been corrected for autooxidation.

3.3. ESR-based quantification of oxidative signals using spin probes

All spin probes exhibited the characteristic three-line spectrum of nitroxide radicals (figure 7). Of the three spin probes tested, CMH was most prone to autoxidation, which may limit its suitability for precise and reproducible measurements, even with background correction. After subtraction of the respective autoxidation signal, all three spin probes showed spin concentrations within a comparable range under identical irradiation conditions.

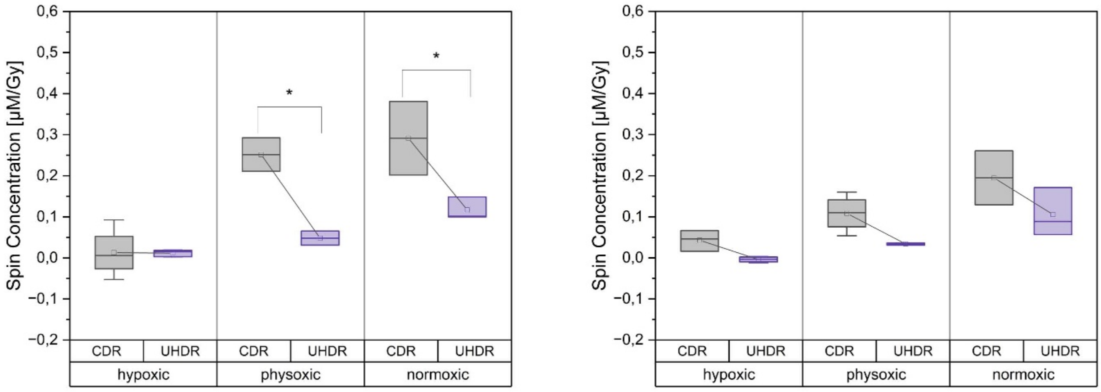

(a) CAT1H pH 4

(b) TMTH pH 4

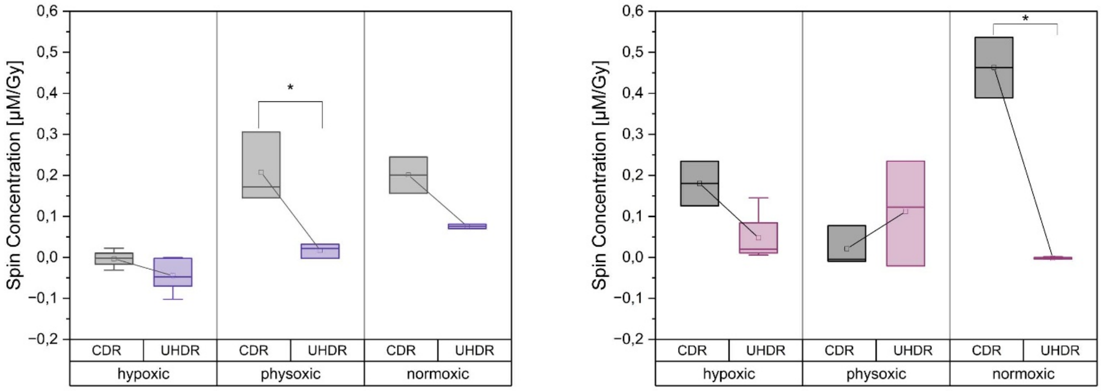

(c) CMH pH 4

(d) CAT1H pH 7.4

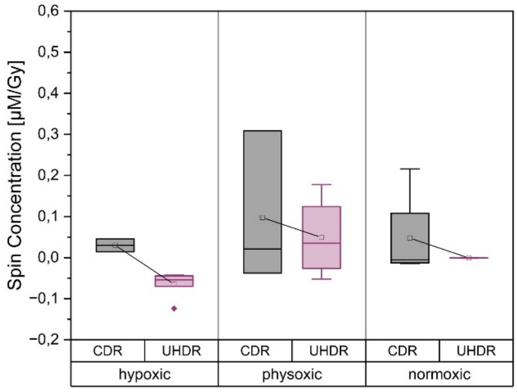

(e) TMTH pH 7.4

Figure 8. Dose-normalised spin adduct concentrations measured with three spin probes (CAT1H, TMTH, CMH) at pH 4, and two probes (CAT1H, TMTH) at pH 7.4, under different oxygenation levels (hypoxic, physioxic, normoxic) and dose rates (CDR, UHDR). Box plots represent median (horizontal line), interquartile range (box), and total spread (whiskers). Asterisks indicate statistically significant differences between conditions (* $p < 0.05$) according to two-way ANOVA with Tukey post-hoc tests. Replicate counts per condition are listed in table S6 (supplementary materials). Differences in whisker length reflect both experimental variability and unequal sample sizes.

Grouped box plots of the dose-normalised spin adduct concentrations are shown in figure 8. The data compare different spin probes under matched conditions of oxygenation (hypoxic, physioxic, normoxic) and dose rate (CDR vs UHDR). The spin-probe measurements showed a certain degree of scatter, which likely reflects the technical limits of the current ESR setup. Future experiments will aim to improve reproducibility by refining oxygen control, optimising ESR measurement timing, and increasing the number of replicates. These measures are expected to further reduce variability across both spin-trap and spin-probe datasets. An increase in spin concentration with increasing oxygen concentration was observed across all spin probes. This effect is largely attributable to the enhanced formation of $O_2^{\bullet -}$, which directly oxidise cyclic hydroxylamines such as CMH, TMTH, and CAT1H to stable nitroxides detectable by ESR. The underlying mechanism involves the reaction of e_{aq}^- with O_2, producing $O_2^{\bullet -}$ in higher yield under normoxic conditions.

Table 5. ANOVA p-values for spin probe experiments at different pH levels. Significant results ($p < 0.05$) are shown in bold. Columns correspond to initial oxygen concentration ($O_{2,\mathrm{initial}}$), mean dose rate (Mean DR), and their interaction ($O_{2,\mathrm{initial}} \times$ DR). Significant main effects for $O_{2,\mathrm{initial}}$ were further analysed using Tukey's HSD post-hoc tests (see table S8 in the Supplementary Materials).

Spin Probe (pH)	$O_{2,\mathrm{initial}}$	Mean DR	$O_{2,\mathrm{initial}} \times$ Mean DR
CAT1H (pH 4)	**$p < 0.0001$**	**$p = 0.00042$**	**$p = 0.0089$**
CAT1H (pH 7.4)	**$p = 0.0094$**	**$p = 0.00061$**	**$p = 0.00016$**
TMTH (pH 4)	**$p = 0.00065$**	**$p = 0.0037$**	**$p = 0.683$**
TMTH (pH 7.4)	$p = 0.232$	$p = 0.131$	$p = 0.873$
CMH (pH 4)	**$p < 0.0001$**	**$p = 0.00016$**	**$p = 0.030$**

However, spin probes are not strictly selective and can also be oxidised by other ROS. As a result, while $O_2^{\bullet-}$ likely dominates the ESR signal under increasing oxygenation, contributions from other oxidants cannot be excluded. In addition to the effects of oxygenation, a dose rate-dependent trend was observed, particularly under acidic conditions. At pH 4, spin probe signals were consistently lower following UHDR compared to CDR, suggesting that high instantaneous radical densities may enhance recombination or introduce competing reaction pathways that reduce net probe oxidation.

Two-way ANOVA results for the dose-normalised spin adduct concentrations are summarised in table 5. The analysis revealed that for CAT1H, both the oxygenation level and the dose rate, as well as their interaction, had a statistically significant effect on the measured spin concentration at both pH 7.4 and pH 4. In contrast, TMTH showed no statistically significant dependence on either factor at pH 7.4, at pH 4, both oxygenation and dose rate emerged as significant contributors to the observed signal variation, although no significant interaction between the two factors was detected. For CMH, which was only tested at pH 4, significant effects of oxygenation level, dose rate, and their interaction were observed.

Negative spin concentrations resulted from the subtraction of the nonirradiated blank signal. These values occurred more frequently under hypoxic UHDR conditions, despite lower oxygen consumption compared to CDR samples. This finding proves that the differences in spin concentration are not due to varying degrees of autoxidation. If autoxidation were the dominant contributor to the observed signals, one would expect lower spin concentrations in CDR samples, where oxygen is more strongly depleted, which was not observed. Importantly, measurements were conducted over variable time intervals after irradiation, with no systematic timing bias between dose-rate groups. In many cases, spectra were acquired several minutes to hours post-irradiation. This makes it improbable that the shorter irradiation duration under UHDR conditions limited autoxidation in a way that could explain the observed differences. Instead, the consistently reduced spin signals under UHDR support the interpretation that radical–radical recombination or other non-oxidative decay pathways are more prominent at high dose rates. These mechanisms likely reduce the pool of free radicals available for spin probe oxidation. Thus, the observed trends reflect fundamental dose-rate-dependent differences in radical dynamics, rather than artefacts of oxygen availability or spontaneous probe oxidation.

This interpretation aligns with previous mechanistic analyses, by Boscolo *et al* (2020), Jansen *et al* (2022b), who showed that elevated dose rates increase the transient concentration of short-lived species such as e^-_{aq} and $H^\bullet$. Since all samples received the same absorbed dose, the total number of radicals generated is assumed to be the same because the dose rate does not affect the total number of primary radicals formed, but rather their temporal distribution.

At high local concentrations, self-reactions such as:

$$e^-_{aq} + e^-_{aq} + 2H_2O \rightarrow H_2 + 2OH^- \tag{3}$$

$$H^\bullet + H^\bullet \rightarrow H_2 \tag{4}$$

can compete with or outpace oxygen-dependent reactions such as:

$$e^-_{aq} + O_2 \rightarrow O_2^{\bullet-} \tag{5}$$
$$H^\bullet + O_2 \rightarrow HO_2^\bullet. \tag{6}$$

As a result, fewer radicals remain to react with O_2 or spin probes, leading to reduced oxygen depletion and lower ESR signals. In particular, the reduced availability of e^-_{aq} to react with O_2 diminishes the formation of $O_2^{\bullet -}$, which directly translates into a weaker ESR signal from superoxide. This highlights a dose-rate-dependent shift in radical dynamics, which favours early recombination under UHDR conditions.

4. Conclusion

This study investigated the influence of dose rate and oxygenation on radical formation during water radiolysis, using both spin traps and spin probes under CDR and UHDR irradiation conditions. While the total absorbed dose was kept constant across all experiments, radical detection varied significantly depending on the oxygen level and dose rate. Spin probe signals and oxygen depletion were consistently reduced under UHDR conditions, suggesting that early radical–radical recombination and other non-oxidative loss mechanisms limit the pool of reactive species available for subsequent oxidative reactions.

In contrast, spin trap-based detection revealed no significant dose rate dependent differences but were likely influenced by kinetic factors such as adduct stability and reaction timing.

These findings emphasise that spin trapping based radical detection is highly sensitive to both chemical and temporal dynamics, particularly under UHDR conditions. These results demonstrate that spin traps and spin probes provide complementary but not equivalent views on radical chemistry, and that quantitative comparisons require careful consideration of probe chemistry, radical lifetimes, and the temporal structure of dose delivery. Overall, our findings strengthen the mechanistic basis for radical–radical recombination-driven explanations of the Flash effect and highlight the need for carefully matched detection strategies in radical chemistry studies. By establishing mechanistic and methodological insights in a controlled chemical setting, this work lays the foundation for studies in more complex biological environments. Future studies could extend these measurements where interactions with cellular components and endogenous scavengers become increasingly relevant. In parallel, supplementing solution studies with biologically representative molecules would help to approximate tissue-like conditions. Ultimately, translation into whole-organism models such as ZFE will be necessary to capture the interplay of radical chemistry with tissue architecture and oxygen gradients under UHDR irradiation.

Data availability statement

All data that support the findings of this study are included within the article (and any supplementary information files).

Supplementary Material available at https://doi.org/10.1088/1361-6560/ae2db6/data1.

Acknowledgments

Parts of this research were carried out at ELBE at the Helmholtz-Zentrum Dresden-Rossendorf e. V, a member of the Helmholtz Association. We thank the ELBE crew for beam preparation and experiment support, Michael Schürer for preparation of the irradiation setup, Elisabeth Leßmann, Artem Govorukhin, and Marvin Apel for their support during the beamtime, Erik Bründermann and the Institute for Beam Physics and Technology (IBPT) at KIT for providing a flashDiamond detector, and Elsa Muller and Axel Klix for technical assistance during experiment preparation.

ORCID iDs

Johanna Pehlivan 0009-0001-2239-0121
Elke Beyreuther 0000-0002-0582-1444
Felix Horst 0000-0003-0707-0856
Michael J Nasse 0000-0001-9260-8205
Jörg Pawelke 0000-0003-4128-5498
Dieter Leichtle 0000-0003-1741-5061
Oliver Jäkel 0000-0002-6056-9747
Bernhard Holzapfel 0000-0002-8420-4777

References

Bačić G, Spasojević I, Šećerov B and Mojović M 2008 Spin-trapping of oxygen free radicals in chemical and biological systems: new traps, radicals and possibilities *Spectrochim. Acta A* **69** 1354–66

Biller J R, Tseitlin M, Mitchell D G, Yu Z, Buchanan L A, Elajaili H, Rosen G M, Kao J P Y, Eaton S S and Eaton G R 2015 Improved sensitivity for imaging spin trapped hydroxyl radical at 250 MHz *ChemPhysChem* **16** 528–31

Boscolo D, Krämer M, Fuss M C, Durante M and Scifoni E 2020 Impact of target oxygenation on the chemical track evolution of ion and electron radiation *Int. J. Mol. Sci.* **21** 424

Bourgouin A, Knyziak A, Marinelli M, Kranzer R, Schüller A and Kapsch R-P 2022 Characterization of the PTB ultra-high pulse dose rate reference electron beam *Phys. Med. Biol.* **67** 085013

Brand M, Granato M and Nüsslein-Volhard C 2002 Keeping and raising zebrafish *Zebrafish* ed C Nüsslein-Volhard and R Dahm (Oxford University Press) pp 7–38

Bruker BioSpin 2022 EPR Detection of the Superoxide Free Radical with the Nitrone Spin Traps DMPO and BMPO (available at: www.bruker.com/de/products-and-solutions/mr/epr-instruments/epr-research-instruments/ELEXSYS-E780.html)

Buxton G V, Greenstock C L, Helman W P and Ross A B 1988 Critical review of rate constants for reactions of hydrated electrons, hydrogen atoms and hydroxyl radicals OH/ O- in aqueous solution *J. Phys. Chem. Ref. Data* **17** 513–886

Cao X *et al* 2021 Quantification of oxygen depletion during FLASH irradiation *in vitro* and *in vivo Int. J. Radiat. Oncol. Biol. Phys.* **111** 240–8

CMH 2025 *CMH Spin Probe—Product Data Sheet* (available at: www.noxygen.de/pages-productinfo/product-80/noxygen-cmh-100mg.html)

Dikalov S I, Kirilyuk I A, Voinov M and Grigor'ev I A 2011 EPR detection of cellular and mitochondrial superoxide using cyclic hydroxylamines *Free Rad. Res.* **45** 417–30

El Khatib M *et al* 2022 Ultrafast tracking of oxygen dynamics during proton FLASH *Int. J. Radiat. Oncol. Biol. Phys.* **113** 624–34

Epel B *et al* 2019 Oxygen-guided radiation therapy *Int. J. Radiat. Oncol. Biol. Phys.* **103** 977–84

Faraggi M, Carmichael A and Riesz P 1984 OH radical formation by photolysis of aqueous porphyrin solutions. a spin trapping and e.s.r. study *Int. J. Radiat. Biol. Relat. Stud. Phys. Chem. Med.* **46** 703–13

Favaudon V *et al* 2014 Ultrahigh dose-rate FLASH irradiation increases the differential response between normal and tumor tissue in mice *Sci. Trans. Med.* **6** 24593

Finkelstein E, Rosen G M and Rauckman E J 1980 Spin trapping of superoxide and hydroxyl radical: practical aspects *Arch. Biochem. Biophys.* **200** 1–16

Frejaville C, Karoui H, Tuccio B, Moigne F L, Culcasi M, Pietri S, Lauricella R and Tordo P 1995 5-(Diethoxyphosphoryl)-5-methyl-1-pyrroline N-oxide: A New Efficient Phosphorylated Nitrone for the in Vitro and in Vivo Spin Trapping of Oxygen-Centered Radicals *J. Med. Chem.* **38** 258–65

Gabriel F, Gippner P, Grosse E, Janssen D, Michel P, Prade H, Schamlott A, Seidel W, Wolf A and Wünsch R 2000 The rossendorf radiation source ELBE and its FEL projects *Nucl. Instrum. Methods Phys. Res. B* **161–163** 1143–7

Giamello G and Brustolon M 2009 *Electron Paramagnetic Resonance: A Practitioner's Toolkit* (Wiley)

Goldstein S, Rosen G M, Russo A and Samuni A 2004 Kinetics of Spin Trapping Superoxide, Hydroxyl and Aliphatic Radicals by Cyclic Nitrones *J. Phys. Chem. A* **108** 6679–85

Gotham J P, Li R, Tipple T E, Lancaster J R, Liu T and Li Q 2020 Quantitation of spin probe-detectable oxidants in cells using electron paramagnetic resonance spectroscopy: To probe or to trap? *Free Radic. Biol. Med.* **154** 84–94

Hawkins C L and Davies M J 2014 Detection and characterisation of radicals in biological materials using EPR methodology *Biochim. Biophys. Acta* **1840** 708–21

Horst F, Bodenstein E, Brand M, Hans S, Karsch L, Lessmann E, Löck S, Schürer M, Pawelke J and Beyreuther E 2024 Dose and dose rate dependence of the tissue sparing effect at ultra-high dose rate studied for proton and electron beams using the zebrafish embryo model *Radiother. Oncol.* **194** 110197

Hosonuma M and Yoshimura K 2023 Association between pH regulation of the tumor microenvironment and immunological state *Front. Oncol.* **13** 1175563

Jansen J, Beyreuther E, García-Calderón D, Karsch L, Knoll J, Pawelke J, Schürer M and Seco J 2022a Changes in Radical Levels as a Cause for the FLASH effect: impact of beam structure parameters at ultra-high dose rates on oxygen depletion in water *Radiother. Oncol.* **175** 193–6

Jansen J, Knoll J, Beyreuther E, Pawelke J, Skuza R, Hanley R, Brons S, Pagliari F and Seco J 2022b Does FLASH deplete oxygen? Experimental evaluation for photons, protons and carbon ions *Med. Phys.* **48** 3982–90

Karsch L *et al* 2022 Beam pulse structure and dose rate as determinants for the flash effect observed in zebrafish embryo *Radiother. Oncol.* **173** 49–54

Khan N, Wilmot C M, Rosen G M, Demidenko E, Sun J, Joseph J, O'Hara J, Kalyanaraman B and Swartz H M 2003 Spin traps: *In vitro* toxicity and stability of radical adducts *Free Radic. Biol. Med.* **34** 1473–81

Khramtsov V V, Grigor'ev I A, Lurie D J, Foster M A, Zweier J L and Kuppusamy P 2004 Spin pH and SH probes: enhancing functionality of EPR-based techniques *J. Spectrosc.* **18** 213–25

Kranzer R, Schüller A, Bourgouin A, Hackel T, Poppinga D, Lapp M, Looe H K and Poppe B 2022 Response of diamond detectors in ultra-high dose-per-pulse electron beams for dosimetry at FLASH radiotherapy *Phys. Med. Biol.* **67** 075002

Labarbe R, Hotoiu L, Barbier J and Favaudon V 2020 A physicochemical model of reaction kinetics supports peroxyl radical recombination as the main determinant of the FLASH effect *Radiother. Oncol.* **153** 303–10

Limoli C L and Vozenin M-C 2023 Reinventing Radiobiology in the light of FLASH Radiotherapy *Ann. Rev. Cancer Biol.* **7** 1–21

Madden K P and Taniguchi H 1996 *In Situ* Radiolysis time-resolved esr studies of spin trapping by dmpo: reevaluation of hydroxyl radical and hydrated electron trapping rates and spin adduct yields *J. Phys. Chem.* **100** 7511–6

Madden K P and Taniguchi H 2001 The role of the DMPO-hydrated electron spin adduct in DMPO-OH spin trapping *Free Radic. Biol. Med.* **30** 1374–80

Pawelke J, Brand M, Hans S, Hideghéty K, Karsch L, Lessmann E, Löck S, Schürer M, Szabó E R and Beyreuther E 2021 Electron dose rate and oxygen depletion protect zebrafish embryos from radiation damage *Radiother. Oncol.* **158** 7–12

Pratx G and Kapp D S 2019 A computational model of radiolytic oxygen depletion during FLASH irradiation and its effect on the oxygen enhancement ratio *Phys. Med. Biol.* **64** 185005

Schuler R H, Neta P and Fessenden R W 1971 Electron spin resonance study of the rate constants for reaction of hydrogen atoms with organic compounds in aqueous solution *J. Phys. Chem.* **75** 1654–66

Sonntag C 2006 *Free-Radical-Induced DNA Damage and Its Repair: A Chemical Perspective (Springerlink BüCher)* (Springer)

Subiel A, Bourgouin A, Kranzer R, Peier P, Frei F, Gomez F, Knyziak A, Fleta C, Bailat C and Schüller A 2024 Metrology for advanced radiotherapy using particle beams with ultra-high dose rates *Phys. Med. Biol.* **69** 14TR01

Sunnerberg J P *et al* 2024 Oxygen Consumption *in vivo* by ultra-high dose rate electron irradiation depends upon baseline tissue oxygenation *Int. J. Radiat. Oncol. Biol. Phys.* **121** S0360301624035107

Villoing D *et al* 2022 Technical note: Proton beam dosimetry at ultra-high dose rates (FLASH): evaluation of GAFchromic™ (EBT3, EBT-XD) and OrthoChromic (OC-1) film performances *Med. Phys.* **49** 2732–45